





Ultrawide field, distortion-corrected ocular shape estimation with MHz optical coherence tomography (OCT)

BINGYAO TAN,^{1,2,3,11}  RYAN P. McNABB,^{4,11}  FEIHUI ZHENG,²
YIN CI SIM,²  XINWEN YAO,^{1,2,3}  JACQUELINE CHUA,^{1,2,5}
MARCUS ANG,^{2,5} QUAN V. HOANG,^{2,5,6,7} ANTHONY N. KUO,^{2,4} AND
LEOPOLD SCHMETTERER^{1,2,3,5,8,9,10,12}

¹SERI-NTU Advanced Ocular Engineering (STANCE), Singapore, Singapore

²Singapore Eye Research Institute, Singapore National Eye Centre, Singapore, Singapore

³School of Chemical and Biomedical Engineering, Nanyang Technological University, Singapore, Singapore

⁴Duke University Medical Center, Durham, NC 27607, USA

⁵Department of Ophthalmology, Duke-NUS Medical School, Singapore

⁶Department of Ophthalmology, Yong Loo Lin School of Medicine, National University of Singapore, Singapore

⁷Department of Ophthalmology, Edward S. Harkness Eye Institute, Columbia College of Physicians and Surgeons, New York, NY 10032, USA

⁸Department of Clinical Pharmacology, Medical University of Vienna, Vienna, Austria

⁹Center for Medical Physics and Biomedical Engineering, Medical University of Vienna, Vienna, Austria

¹⁰Institute of Molecular and Clinical Ophthalmology, Basel, Switzerland

¹¹Authors contributed equally to the study.

¹²leopold.schmetterer@seri.com.sg

Abstract: Ocular deformation may be associated with biomechanical alterations in the structures of the eye, especially the cornea and sclera in conditions such as keratoconus, congenital glaucoma, and pathological myopia. Here, we propose a method to estimate ocular shape using an ultrawide field MHz swept-source optical coherence tomography (SS-OCT) with a Fourier Domain Mode-Locked (FDML) laser and distortion correction of the images. The ocular biometrics for distortion correction was collected by an IOLMaster 700, and localized Gaussian curvature was proposed to quantify the ocular curvature covering a field-of-view up to $65^\circ \times 62^\circ$. We achieved repeatable curvature shape measurements (intraclass coefficient = 0.88 ± 0.06) and demonstrated its applicability in a pilot study with individuals ($N = 11$) with various degrees of myopia.

© 2021 Optical Society of America under the terms of the [OSA Open Access Publishing Agreement](#)

1. Introduction

Ocular deformation may be associated with biomechanical alterations in the structures of the eye, especially the cornea and sclera in conditions such as keratoconus [1,2] and pathologic myopia [3,4]. Severe alterations in ocular shape can lead to pathological changes in ocular structures, for example, the formation of posterior staphyloma in pathological myopia, where the outpouching of the sclera leads to abnormalities of the retinal pigment epithelium (RPE), retina, and choroid. Thus, monitoring the changes in the ocular shape of myopic eyes may be useful in detecting early structural changes, before damage and visual impairment occur with the development of actual staphyloma.

However, imaging the entire eye to assess its ocular shape is currently problematic [4]. Conventionally, magnetic resonance imaging (MRI) may be used [5–9], but this approach has many disadvantages: it is bulky, costly, time-consuming, yields low, anisotropic resolution, and uncomfortable and/or contraindicated for some patients. As MRI machines are not readily accessible in many eye clinics, this modality is not currently used as part of routine ocular

imaging and assessment. Other approaches, such as ultrasonography [10,11], partial coherence interferometer [12,13], and peripheral refraction [14], have limited sampling rates or resolutions. Optical coherence tomography (OCT) can provide a volumetric representation of the posterior pole with optical resolution and an acquisition time within seconds [15]. In particular, swept-source OCT (SS-OCT) provides a better signal roll-off and larger imaging depth than spectral-domain OCT. With the recent development of megahertz (MHz) swept-source engines, including Fourier domain mode-locked (FMDL) lasers and vertical-cavity surface-emitting lasers (VCSEL), a dense-sampling volumetric scan can be acquired within a cardiac cycle.

A commercial ultrawide field SS-OCT system (Canon, Japan) can scan a field of view up to $23 \times 20 \text{ mm}^2$ on the retina, thus it enables detection of wide staphyloma [16–18]. However, it remains challenging to measure the actual changes of the ocular shape because of the optical distortions that are inherent to OCT imaging: several measures, such as the distance between machine and eye for a given exam can significantly alter the ocular shape displayed in OCT images. To solve this problem, McNabb et al. developed a whole eye system to simultaneously image the anterior and posterior eye [19]. A ray-tracing model was then used to reconstruct the true retinal shape. Later, the same group proposed a sparse radial scan pattern to cover a disk area 12 mm in diameter at the posterior pole. However, limited by the system speed (100/200kHz), the curvature can be quantified only along each radial B-scan, and a tomogram of the retinal curvature was generated via interpolating the radial scans [20]. Additionally, a similar approach was also applied to commercial devices and yielded comparable results to MRI scans [21], but the knowledge of the optical parameters was not fully known, making inter-scan or inter-patient comparisons difficult.

Based on these limitations, we propose a method to estimate the ocular curvature using a MHz SS-OCT with an FMDL laser and an ultrawide field optical design. The ocular biometrics for distortion correction was collected by IOL Master 700, and a localized Gaussian curvature was proposed to quantify the ocular curvature up to $65^\circ \times 62^\circ$. We also tested its repeatability and demonstrated its applicability in a pilot study with individuals ($N = 11$) with various degrees of myopia. The ability to quantify ocular shape can allow for a more objective staging of posterior staphyloma in pathological myopia and its progression.

2. Method

2.1. OCT system and imaging protocols

An optical schematic of the MHz FMDL SS-OCT system (Optores, Munich, Germany) is shown in Fig. 1, and a photograph of the patient interface module is shown in the inset. Briefly, the light source is an FMDL laser (central wavelength: 1061 nm, bandwidth: 75 nm; Optores, Munich, Germany) operated at a 1.66 MHz A-line rate. A calibration arm was integrated to generate a monotone with the reference arm for the linear-k resampling. A Hilbert transform was applied to the interference fringes, where the nonlinearity of the phase was resampled by linear interpolation. The switch between calibration and eye imaging was controlled by an electrical shutter in the calibration arm. The coefficients of the k-space resampling were applied to the retinal images, and the coefficients remained relatively stable throughout the imaging session. The sample arm consisted of a collimator, a pair of galvo scanners (6215H, Cambridge Technology, MA, USA), and customized telescope lenses ($f_1 = 91.0 \text{ mm}$, $f_2 = 42.0 \text{ mm}$) intended to minimize the eye aberration and light transmission at a large oblique incident angle [21]. The ocular lens design catered for ultrawide imaging up to 100° in emmetropic eyes, but a smaller FOV is more suitable for myopia. An iris camera and a fixation target ($\lambda = 635 \text{ nm}$, $P = 7 \mu\text{W}$) were integrated for eye alignment and fixation, respectively. A dual-channel balanced photodetector (WL-BPD1GA, Wieserlabs, Munich, Germany) and a PCIe based digitizer (ATS9373, Alazar Technologies Inc., Montreal, Canada) were employed for fringe detection and digitization. The digitizer operated at 3.68 GS/s clocked internally, sampling 2304 points for each sweep cycle, providing an imaging

range of 4.2 mm and >6 mm 6-dB signal roll-off. The sensitivity roll-off was dominated by the limited bandwidth of the photodetector [22]. The axial resolution was $4.7\ \mu\text{m}$ in tissue, and the lateral resolution was approximately $45\ \mu\text{m}$ measured on a USAF resolution target (Thorlabs, Newton, NJ, USA) in a model eye (E-106-1, Epipole, UK). The beam size at the pupil was 1.3 mm. The signal-to-noise ratio was 95 dB with an incident power of 3.0 mW onto the cornea, which together with the power from the fixation target was below the maximum permissible exposure (ANSI Z80.36-2016). A data acquisition software (Optores, Germany) with real-time B-scan display was used for in-vivo image alignment.

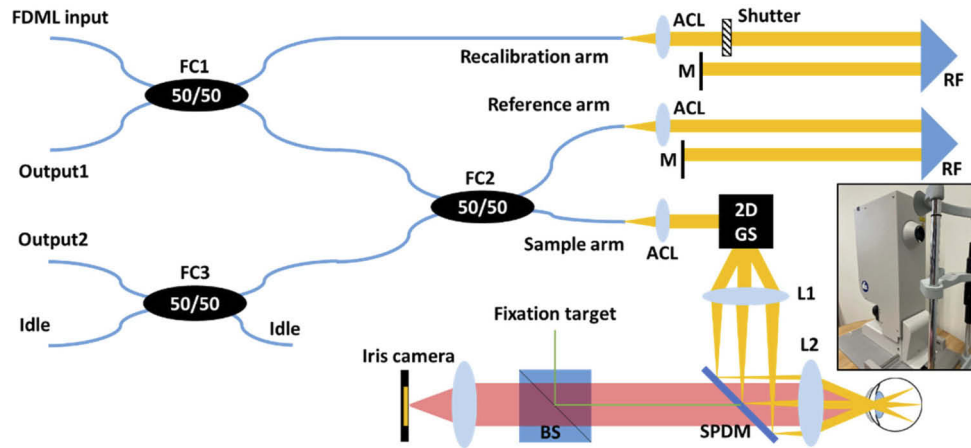


Fig. 1. The schematic of the MHz SS-OCT system. Inset: The photograph of the patient interface. FDML: Fourier domain mode-locked. FC: fiber coupler. ACL: achromatic lens. M: mirror. L: customized lens. 2D-GS: two-dimensional galvo scanners. SPDM: short pass diachronic mirror. BS: beam splitter. RF: retroreflector.

For the scan protocol, the field of view (FOV) was 65° in the fast scan direction and 62° in the slow scan direction. The calibration of the FOV was conducted based on a customized phantom eye with a 3D printed bowl-shaped plastic target (next section). Each volume consisted of 1536 A-scans and 993 B-scans. The acquisition time for each volume was approximately 1.6s, with a duty cycle of 60% on the fast scanner. The image was oriented such that deeper ocular structures were closer to DC to improve sensitivity in the macular region.

A total of 11 eyes from 11 normal subjects (34.8 ± 8.7 years old, range: 25-56 years old) with different degrees of myopia were recruited from Singapore National Eye Center and imaged in triplicate without mydriasis and with a 1-minute interval between images. The room light was turned on to constrict the pupil size for better alignment of the pivotal point with respect to the pupil. Ocular biometrics, including axial eye length, central corneal thickness, and corneal curvature were later acquired by IOLMaster 700 (Zeiss Meditec, CA, USA).

2.2. System calibration

A customized eye phantom (Fig. 2) was utilized to calibrate the scan FOV. It consisted of a 3D printed iris (3 mm diameter), an achromatic doublet (AC127-025-C, Thorlabs, USA), and a plastic target with a bowl-shaped surface, 3D printed from a stereolithography printer (Form 3, FormLab, USA). The curvature of the surface was designed to be 13.00 mm, with four rows of markers extruding $100\ \mu\text{m}$ vertically from the surface. The interval between the markers was 1 mm in the transverse direction. A spacer was placed in between the doublet and the plastic target to place the target at the focal plane of the lens.

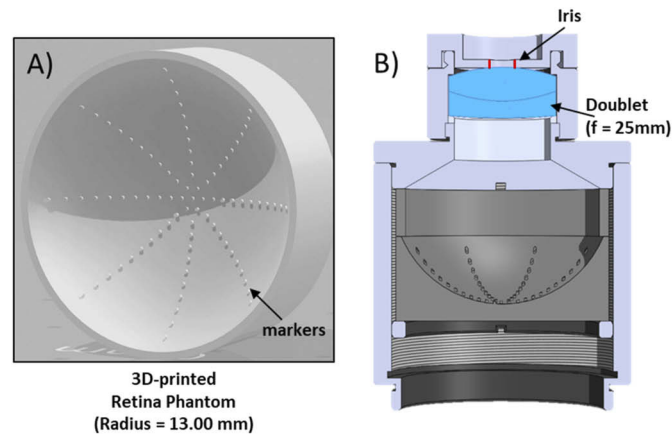


Fig. 2. A) A 3D rendering of the printed plastic target with a bow shape surface and four rows of markers extruding from the surface ($R_c = 13.00$ mm). B) A cross-sectional view of the phantom eye.

The plastic surface was imaged with the beam pivot carefully placed at the iris center. The raster scan directions were aligned to two orthogonal rows of markers. The image volume was then compressed onto an elevation map by identifying the location of the maximal intensity along each A-scan. Loci of the markers were pinned manually from the map, and their corresponding scanning angles θ_n were calculated as $\tan^{-1}(X_n/Y_n)$, where X_n and Y_n were the horizontal and vertical distances from the n th marker to the pivot, respectively. Subsequently, the relationship between the scanning angle and marker loci showed that the scan location was linearly correlated with the scan angle and minimally affected by the galvo scanner jitter. By extrapolating the linear relation to the image boundaries, the FOV of the scanning protocol was determined.

2.3. Distortion correction via ray tracing

The distortion was corrected by modeling the beam propagation in the sample arm (OpticStudio, ZEMAX). The detailed method has been described elsewhere [19,23]. Briefly, optical parameters, including the surface, material, and distance information from galvo scanners, telescope lenses, and human eyes were incorporated into the model, and a Polans eye model [24] was utilized to represent the human eye, where corneal thickness, anterior chamber depth and axial eye length were measured from the IOLMaster 700. The ray-tracing model allowed for simulating the beam scanning by rotating the x- and y- galvo scanners. The optical path length (OPL) between the x-galvo scanner and the retinal surface was then calculated for each incident angle. A total of 300×200 incident angles along with the fast and slow directions respectively were stimulated for each eye.

The models of one short eyeball and one long eyeball are shown in Fig. 3. Blue lines with arrows indicate the chief ray propagation to the retina, with one normal to the eye and two oblique ones representing the boundaries of the scanning FOV. It is apparent that identical scanning angles yielded a larger scanning area on a longer eyeball.

2.4. Image post-processing

The RPE layer over the entire volume was segmented automatically based on graph theory and dynamic programming [25,26]. The RPE layer on a central scan was initially segmented, and a band 20 pixels above and underneath the RPE layer was utilized as a region of interest for the neighboring scans. This procedure was iterated and propagated to the entire volume.

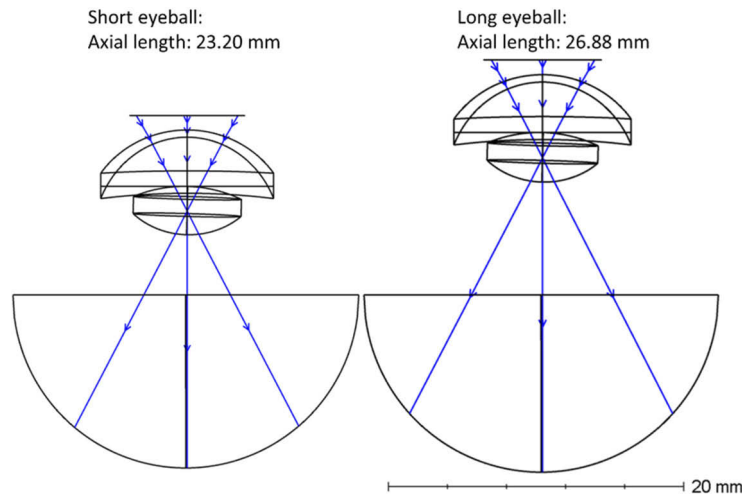


Fig. 3. Eye models with different axial eye lengths. Blue lines: Chief rays incident from different angles. Note that in the eye with the longer axial length, the scan width is larger than that of the shorter eye.

Although the MHz rate of the SS-OCT engine effectively reduces the volumetric acquisition time, motion artifacts were still present that can affect high-order ocular shape descriptors. These motion artifacts, originated from a variety of linear and non-linear motions, including translation, rotation, and pulsatile expansion/contraction were difficult to isolate. To address these artifacts, we propose a simplified motion estimation and compensation method. First, before distortion correction, profiles of the RPE elevation along the slow scan direction were extracted, at the locations 3 mm nasally and temporally eccentric to the fovea. Second, a 7th order polynomial function fits each profile with a *bisquare* optimization, where the residuals were calculated (L_1 and L_2 in Fig. 4(A)). Last, a residual map was generated by linearly fitting L_1 & L_2 on each slow-scan position (Fig. 4(A)). The black arrow and red arrow labeled the artifacts that most likely represent a translation and a tilt of the eyeball, respectively. The motion artifacts (residues) were removed from the surface, the result of which was then to correct the distortion.

To compensate for any remaining segmentation inaccuracy, we further low pass filtered the retinal surface with 2D polynomial fitting to the 9th order, with *bisquare* optimization. As the ocular shape change from pathology is mostly on a large scale, the high order polynomial fitting only removed the small-scale surface variation while preserving the localized curvature change. The fitting residual was mostly within 20 μ m and partially came from the inaccurate segmentation underneath the large blood vessels in the superficial plexus (Fig. 4(B)).

2.4.1. Curvature quantification

To quantify local retinal shape, we adopted the Gaussian curvature (K), which is an invariant topological parameter previously used to describe the stretch or compression of biological tissue or cells [27]. The Gaussian curvature at point p is calculated as the production of the principal curvatures k_1 and k_2 from two normal sections. An illustration of Gaussian curvature calculation on a saddle function ($Z = X^2 - Y^2$) is shown in Fig. 4(C). The Gaussian function K at the saddle point is less than 0 with $k_1 > 0$ and $k_2 < 0$.

The effects of motion compensation and 2D polynomial fitting on the Gaussian curvature are shown in Fig. 4(D)-(F). Without any compensation, the Gaussian curvature map was deteriorated by motion artifacts, appearing as horizontal stripes (Black arrow, Fig. 4(D)) across the entire FOV. After motion compensation, the horizontal lines were largely removed, but curvature

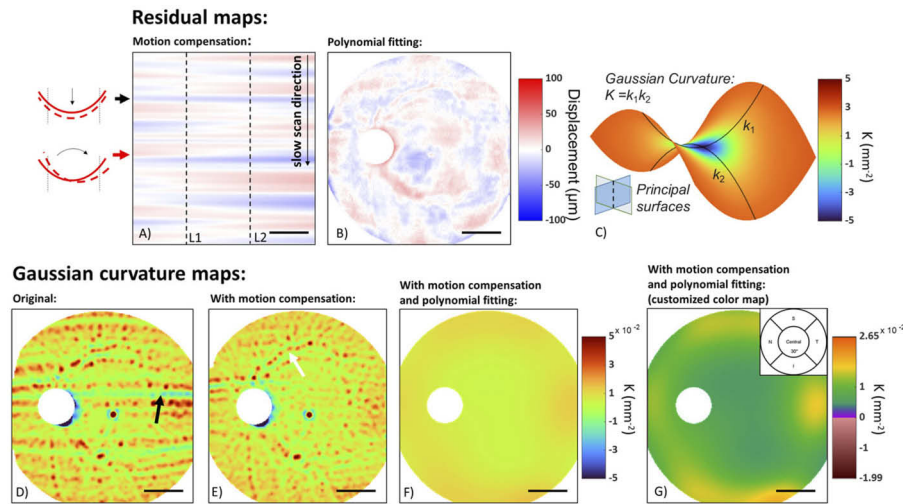


Fig. 4. Effect of motion compensation and polynomial fitting on Gaussian curvature. A) The residual map from motion compensation on the RPE elevation map before distortion correction. Black arrow: artifact from a translation motion. Red arrow: artifact from a tilt. B) Residual map of the 9th order polynomial fitting on the RPE map after distortion correction. C) Gaussian curvature on a saddle function. D) Gaussian curvature map without motion compensation nor polynomial fitting. Black arrow: motion artifacts present as the horizontal stripes across the entire FOV. E) Gaussian curvature map after motion compensation. Localized curvature variation came from inaccurate RPE segmentation partially because of the vessel shadow. F) Gaussian curvature map with motion compensation and 9th order polynomial fitting. G) The same Gaussian curvature map as in F) but shown in a customized color scale. Gaussian curvature was calculated over the entire FOV as well as in each sector (Inset). Scale bar: 5 mm.

variation from the residual motion artifact or segmentation inaccuracies still caused erroneous curvature detection. Notably, some of the errors followed the pattern of the large vessels from the superficial plexus (white arrow, Fig. 4(E)), and the high variation in the fovea was because of a segmentation error (Fig. 4(E)). Further fitting the surface removed local variation while preserving the high-order ocular shape (Fig. 4(F)). A customized colormap [20] was used to enhance the contrast: normal curvature ranges were shown in green, flatter retina was shown in purple, and more concave retina was shown in yellow to orange. A distinct color gradient from purple to pink indicated the transition from concavity to convexity. The entire FOV was separated into five sectors: central 30° sector and four peripheral quadrants (Nasal, Temporal, Superior, Inferior) (Inset in Fig. 4(G)), and the Gaussian curvature was calculated over the entire FOV, as well as in each sector.

3. Result

Figure 5(A) shows an OCT cross-section of the plastic target. Twenty-one markers from one row could be visualized, and printing errors were present on the right side of the image (white arrow). A volumetric OCT view could visualize all the markers (Fig. 5(B)), which were used for FOV calibration. The distortion-corrected target surface is shown in Fig. 5(C). The radius of the curvature of the best-fitted sphere was 12.87 mm, and the Gaussian curvature was $0.0057 \pm 0.00057 \text{ mm}^{-2}$ from all sectors. The designed spherical radius of curvature was 13 mm in SolidWorks, equivalent to Gaussian curvature 0.0059 mm^{-2} . The detected curvature was

well-aligned with the design, and the 2% difference could originate from the limited printing resolution and resin shrinkage during washing and curing.

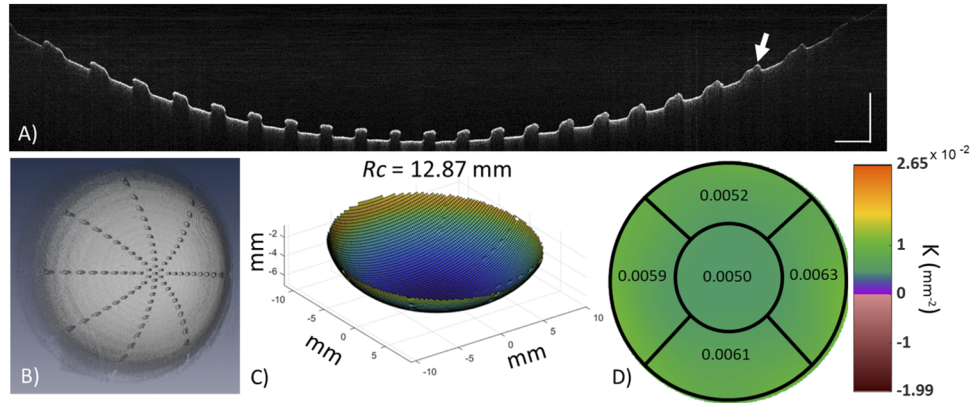


Fig. 5. A) An OCT cross-section of the plastic target. Scale bar: 1 mm. B) The volumetric OCT view of the plastic target. The extruded markers were visualized. C) Distortion corrected surface of the plastic target. The radius of curvature was 12.87 mm, and the design radius of curvature is 13.00 mm. D) Gaussian curvature measurement from the target surface.

Figure 6(A) shows a raw 3D rendered posterior pole centered at fovea from a subject (age: 32 years old, Male; [Visualization 1](#)). The low-intensity regions in the volume edge (white arrow) were due to the light obstructed by the eyelashes. Figure 6(B)-(C) are cross-sectional scans across the optic nerve head and 15° superior to the fovea, respectively. The images were acquired with the choroid placed close to the zero-delay and flipped vertically for visualization purposes. Red lines indicated the results of RPE segmentation, and an animation flying through the entire volume with the RPE segmentation is shown in [Visualization 2](#).

To test the repeatability of the method, a total of 11 eyes from 11 subjects were imaged three times. Figure 7 shows the representative results from one eye (age = 34 years old, female). Visually, the distortion corrected RPE elevation maps and the Gaussian curvature maps showed clear and repeatable patterns: the ocular surface was flatter (smaller K value) superior to the optic nerve head, and more concave (larger K value) along an arc in the inferior and temporal peripheral regions. Among all eyes, the radius of ocular curvature with the best fitted sphere had perfect repeatability (intraclass coefficient (ICC) = 0.96) and Gaussian curvature in different sectors had good to perfect repeatability (ICC: 0.88 ± 0.06), where the nasal region had the lowest ICC value (0.78) and the central 30° the highest (0.94).

Representative Gaussian curvature maps from four eyes are shown in Fig. 8. No ocular disease was diagnosed among these eyes, and they were arranged with increasing axial length and decreasing spherical equivalent. In subjects 1&2, the Gaussian curvature over the entire FOV was around 0.01 mm^{-2} , with slightly more concave regions at some of the peripheral quadrants. In subject 4, the retina was flatter in the macular area, shown in purple color with lower Gaussian curvature. The Gaussian curvature from 11 healthy eyes with different spherical equivalent (-1.00D to -8.00D) and axial eye length (23.18 mm to 26.88 mm) were summarized in Table 1. The radius of ocular curvature was $11.26 \pm 0.31 \text{ mm}$ with the best sphere fitting, equivalent to a Gaussian curvature of 0.0079 mm^{-2} , and the measured Gaussian curvature was $0.0078 \pm 0.0018 \text{ mm}^{-2}$, equivalent to 11.30 mm radius of ocular curvature. It indicated that Gaussian curvature contains a wealth of information regarding not only the radius of the ocular curvature but also, more importantly, higher-order localized curvature.

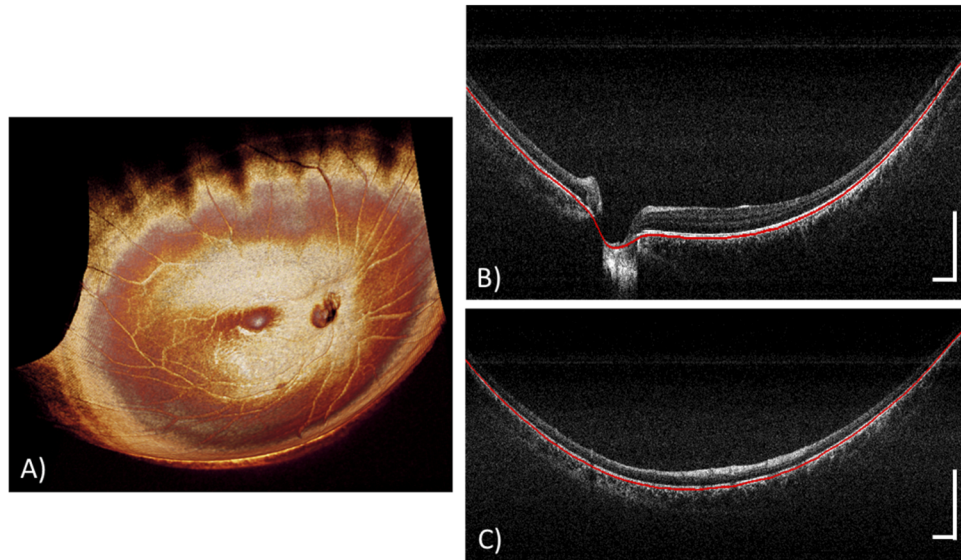


Fig. 6. Ultrawide field posterior eye imaging and RPE segmentation. A) 3D rendering of the volumetric posterior eye, with an estimated field of view $65^\circ \times 62^\circ$. B-C) Cross-sectional scans across the ONH (B) and 15° superior to the fovea (C), with red lines indicating the automatically segmented RPE. 3x consecutive B-scan averaging was used to reduce the background noise. The images were flipped vertically for display convenience. Scale bar: 1 mm.

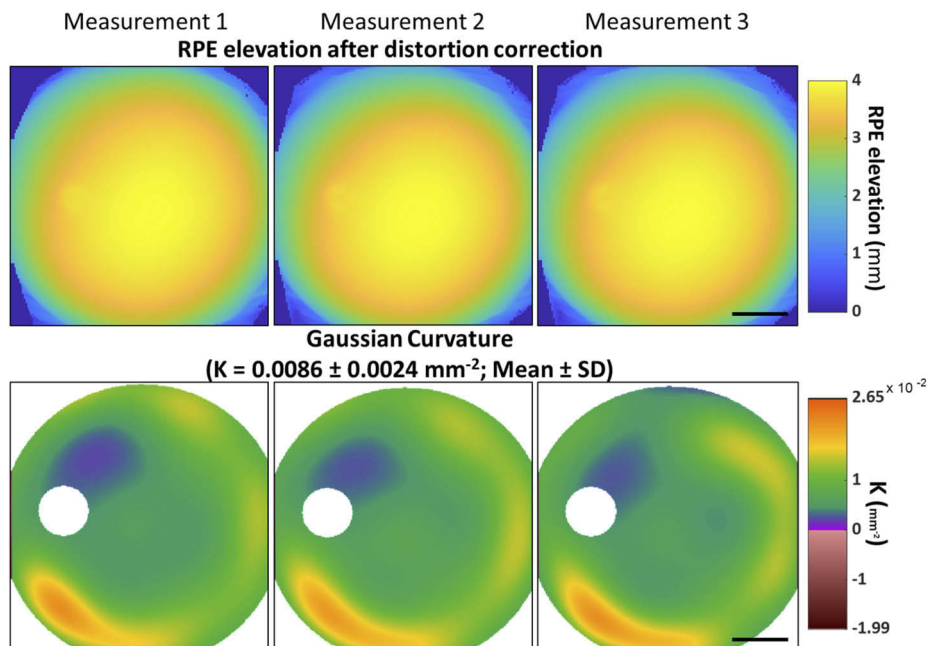


Fig. 7. RPE elevation maps after distortion correction and Gaussian curvature maps from repeated scans. Scale bar: 5 mm.

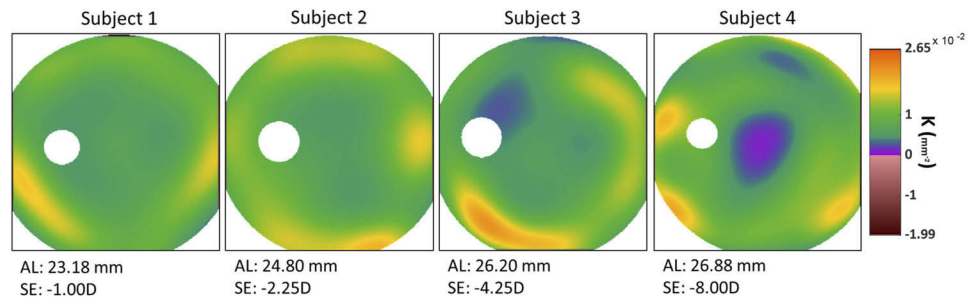


Fig. 8. Gaussian curvature map from four eyes with different axial eye lengths and spherical equivalents, ranging from emmetropia to myopia. AL: axial length. SE: spherical equivalent.

Table 1. Ocular shape quantification

	Central 30 degree	Gaussian Curvature (mm^{-2})				$R_c(\text{mm}^{-1})$
		Superior	Inferior	Nasal	Temporal	
Mean	0.00468	0.0081	0.0086	0.0085	0.0091	11.26
SD	0.00076	0.0012	0.0015	0.0009	0.0009	0.31
ICC	0.94	0.86	0.92	0.78	0.89	0.96

4. Discussion

We demonstrated distortion-corrected ultrawide ocular curvature estimation using a MHz SS-OCT system. A MHz OCT engine could substantially reduce the volumetric acquisition time and subsequently the motion artifacts. A ray-tracing algorithm reconstructed the true ocular shape from OCT scans, and a Gaussian curvature map was proposed here to quantify the localized ocular curvature, which could help us detect macular and peripheral ocular shape abnormalities in various ocular diseases, such as staphyloma in high myopia.

Distortion-corrected ocular curvature detection can identify staphyloma more readily. The commercially available OCTs provide a limited FOV that could erroneously call a steep retina contour (within a 6 or 12 mm scan) a staphyloma [28,29]. The machine-to-eye distance could substantially affect the curvature displayed in OCT images: placing the eye away from the pivot could make the retina more curved. Although full knowledge of the optical parameters in the sample arm is required to reconstruct the true ocular curvature, this technique could also detect relative and longitudinal changes of the retinal curvature on standard OCTs if machine-to-eye distance and ocular biometrics are not available.

Full eye imaging modalities, including B scan ultrasonography [10,11] and MRI [5–7,9,30] are not commonly used in clinics because of low resolution and high demand for operational expertise. Moreover, MRI is costly, time-consuming, and uncomfortable and/or contraindicated for some patients. In more selective cases where there is already the presence of myopic traction maculopathy, the ultrawide field enabled by the MHz OCT (up to $65^\circ \times 62^\circ$) is also beneficial as it has been postulated that peripheral pathologic traction may sometimes be the driving force that results in pathology that manifests in the posterior pole [31–34].

The existing hypothesis is that curvature changes in highly myopic eyes may precede the development of outright staphyloma outpouching, and that asymmetry of curvature may be an early indicator of localized weakness that will eventually result in a staphyloma [3]. The Gaussian curvature change is a resultant of the localized biomechanical properties alteration that the value deviates from the normal distribution is a sign of tissue stretching and compressing, instead of bending (Gauss's remarkable theorem) [27]. Some biomarkers could be extracted

to discern which highly myopic eyes will remain stable versus which highly myopic eyes will progress to pathology with staphyloma formation, myopic traction maculopathy, or myopic macular degeneration. Previous studies have reported a potential role of choroidal thickness and scleral shape in the development of pathologic myopia and myopia-associated optic neuropathy. Integrating the curvature information with these other metrics, such as choroid thickness, sclera thickness, and their biomechanical properties could help us estimate tissue stress to strain relationship and its role in pathological myopia development in the future [35–37].

One limitation of this study is the lack of a precise machine-to-eye distance measure, which as aforementioned, a key parameter in the ray tracing algorithm. Although ultrawide scanning mode without mydriasis allows us to align pivot more accurately (because clipping would occur if the pivot were outside the constricted pupil), the assumption that the pupil center was placed at the pivot could be compromised. The uncertainty in pivotal point alignment could cause 8% and 2% variations in R_c and Gaussian curvature estimations. Potential solutions are incorporating a dual channel for the anterior segment, using an iris camera with a tunable lens to calibrate the machine-to-eye distance, or calibrating the reference arm position during each acquisition. Moreover, while we did not use relay lenses between two scanners, our ray tracing algorithm simulated this non-perfect pupil plane conjugation and corrected for the resulting distortion. Lastly, the vignetting-caused low intensity at the peripheral regions increased the uncertainty of RPE segmentation, where the segmentation errors were manually corrected or excluded for the following quantification.

In conclusion, we propose a method to estimate the ocular curvature using a MHz SS-OCT with a FDML laser and an ultrawide field optical design. High repeatability of the radius of the curvature and Gaussian curvature was achieved. A pilot study tested its applicability on emmetropic and myopic eyes. Future studies will explore its utility in larger myopia cohorts and investigate the ocular biomechanical properties in high myopia.

Funding. National Eye Institute (R01-EY024312); National Institutes of Health; National Medical Research Council (CG/C010A/2017, OFIRG/0048/2017, OFLCG/004c/2018, TA/MOH-000249-00/2018); the Singapore Eye Research Institute & Nanyang Technological University; Agency for Science, Technology and Research (A20H4b0141); National Research Foundation Singapore.

Acknowledgment. We would like to thank Tom Pfeiffer, Thomas Klein, and Wolfgang Wieser from Optores GmbH for their assistance with the system calibration.

Disclosures. The authors declare that there are no conflicts of interest related to this article.

Data availability. Data underlying the results presented in this paper are not publicly available at this time but may be obtained from the authors upon reasonable request.

References

1. D. P. Piñero, J. L. Alió, A. Alesón, M. E. Vergara, and M. Miranda, "Corneal volume, pachymetry, and correlation of anterior and posterior corneal shape in subclinical and different stages of clinical keratoconus," *J. Cataract Refract. Surg.* **36**, 814 (2010).
2. K. Bizheva, B. Tan, B. MacLellan, O. Kralj, M. Hajjalamdari, D. Hileeto, and L. Sorbara, "Sub-micrometer axial resolution OCT for in- vivo imaging of the cellular structure of healthy and keratoconic human corneas," *Biomed. Opt. Express* **8**(2), 800–812 (2017).
3. K. Ohno-Matsui and J. B. Jonas, "Posterior staphyloma in pathologic myopia," *Progress in Retinal and Eye Research* **70**, 99–109 (2019).
4. M. Ang, C. W. Wong, Q. V. Hoang, G. C. M. Cheung, S. Y. Lee, A. Chia, S. M. Saw, K. Ohno-Matsui, and L. Schmetterer, "Imaging in myopia: potential biomarkers, current challenges and future developments," *Br. J. Ophthalmol.* **103**(6), 855–862 (2019).
5. A. N. Kuo, P. K. Verkicharla, R. P. McNabb, C. Y. Cheung, S. Hilal, S. Farsiu, C. Chen, T. Y. Wong, M. Kamran Ikram, C. Y. Cheng, T. L. Young, S. M. Saw, and J. A. Izatt, "Posterior eye shape measurement with retinal OCT compared to MRI," *Investig. Ophthalmol. Vis. Sci.* **57**(9), OCT196 (2016).
6. L. S. Lim, S. Matsumura, H. M. Htoon, J. Tian, S. Bin Lim, S. Sensaki, C. Chen, S. Hilal, T. Y. Wong, C. Y. Cheng, A. Kuo, and S. M. Saw, "MRI of posterior eye shape and its associations with myopia and ethnicity," *Br. J. Ophthalmol.* **104**, 1239 (2020).

7. M. Moriyama, K. Ohno-Matsui, K. Hayashi, N. Shimada, T. Yoshida, T. Tokoro, and I. Morita, "Topographic analyses of shape of eyes with pathologic myopia by high-resolution three-dimensional magnetic resonance imaging," *Ophthalmology* **118**(8), 1626–1637 (2011).
8. K. Ohno-Matsui, "Proposed classification of posterior staphylomas based on analyses of eye shape by three-dimensional magnetic resonance imaging and wide-field fundus imaging," *Ophthalmology* **121**(9), 1798–1809 (2014).
9. Q. V. Hoang, S. Chang, D. J. G. Yu, L. A. Yannuzzi, K. B. Freund, and J. Grinband, "3-D assessment of gaze-induced eye shape deformations and downgaze-induced vitreous chamber volume increase in highly myopic eyes with staphyloma," *Br. J. Ophthalmol.* **105**, 1149 (2020).
10. M. Restori, "Ophthalmic ultrasound: a diagnostic atlas," *Br. J. Ophthalmol.* **84**(8), 936h–936 (2000).
11. D. Doro, S. Visentin, P. E. Maimone, and E. Pilotto, "High-resolution ultrasonography in central serous chorioretinopathy," *Am. J. Ophthalmol.* **139**(3), 550–552 (2005).
12. P. K. Verkicharla, M. Suheimat, J. M. Pope, F. Sepehrband, A. Mathur, K. L. Schmid, and D. A. Atchison, "Validation of a partial coherence interferometry method for estimating retinal shape," *Biomed. Opt. Express* **6**(9), 3235 (2015).
13. C. A. Clark, A. E. Elsner, and B. J. Konynenbelt, "Eye shape using partial coherence interferometry, autorefraction, and SD-OCT," *Optom. Vis. Sci.* **92**(1), 115–122 (2015).
14. G. Zeng, H. E. Bowrey, J. Fang, Y. Qi, and S. A. McFadden, "The development of eye shape and the origin of lower field myopia in the guinea pig eye," *Vision Res.* **76**, 77–88 (2013).
15. W. Drexler and J. G. Fujimoto, *Optical Coherence Tomography: Technology and Applications* (Springer Science & Business Media, 2008).
16. K. Shinohara, N. Tanaka, J. B. Jonas, N. Shimada, M. Moriyama, T. Yoshida, and K. Ohno-Matsui, "Ultrawide-field oct to investigate relationships between myopic macular retinoschisis and posterior staphyloma," *Ophthalmology* **125**(10), 1575–1586 (2018).
17. R. Saito, K. Shinohara, N. Tanaka, H. Takahashi, T. Yoshida, and K. Ohno-Matsui, "Association between dome-shaped macula and posterior staphyloma in highly myopic eyes investigated by ultra-widefield optical coherence tomography," *Retina* **41**(3), 646–652 (2021).
18. K. Shinohara, M. Moriyama, N. Shimada, T. Yoshida, and K. Ohno-Matsui, "Characteristics of peripapillary staphylomas associated with high myopia determined by swept-source optical coherence tomography," *Am. J. Ophthalmol.* **169**, 138–144 (2016).
19. R. P. McNabb, J. Polans, B. Keller, M. Jackson-Atogi, C. L. James, R. R. Vann, J. A. Izatt, and A. N. Kuo, "Wide-field whole eye OCT system with demonstration of quantitative retinal curvature estimation," *Biomed. Opt. Express* **10**(1), 338 (2019).
20. R. P. McNabb, A. S. Liu, S. M. Gospe, M. El-Dairi, L. C. Meekins, C. James, R. R. Vann, J. A. Izatt, and A. N. Kuo, "Quantitative topographic curvature maps of the posterior eye utilizing optical coherence tomography," *Retina* **41**(4), 804–811 (2021).
21. J. P. Kolb, T. Klein, C. L. Kufner, W. Wieser, A. S. Neubauer, and R. Huber, "Ultra-widefield retinal MHz-OCT imaging with up to 100 degrees viewing angle," *Biomed. Opt. Express* **6**(5), 1534 (2015).
22. T. Klein, W. Wieser, L. Reznicek, A. Neubauer, A. Kampik, and R. Huber, "Multi-MHz retinal OCT," *Biomed. Opt. Express* **4**(10), 1890 (2013).
23. A. N. Kuo, R. P. McNabb, S. J. Chiu, M. A. El-Dairi, S. Farsiu, C. A. Toth, and J. A. Izatt, "Correction of ocular shape in retinal optical coherence tomography and effect on current clinical measures," *Am. J. Ophthalmol.* **156**(2), 304–311 (2013).
24. J. Polans, B. Jaeken, R. P. McNabb, P. Artal, and J. A. Izatt, "Asymmetric wide-field optical model of the human eye with tilted and decentered crystalline lens that reproduces experimentally measured aberrations: errata," *Optica* **5**(11), 1461 (2018).
25. P. P. Srinivasan, S. J. Heflin, J. A. Izatt, V. Y. Arshavsky, and S. Farsiu, "Automatic segmentation of up to ten layer boundaries in SD-OCT images of the mouse retina with and without missing layers due to pathology," *Biomed. Opt. Express* **5**(2), 348 (2014).
26. B. Tan, Z. Hosseinaee, and K. Bizheva, "Dense concentric circle scanning protocol for measuring pulsatile retinal blood flow in rats with Doppler optical coherence tomography," *J. Biomed. Opt.* **22**(11), 1 (2017).
27. S. J. P. Callens, R. J. C. Uyttendaele, L. E. Fratila-Apachitei, and A. A. Zadpoor, "Substrate curvature as a cue to guide spatiotemporal cell and tissue organization," *Biomaterials* **232**, 119739 (2020).
28. F. Zheng, C. W. Wong, C. Sabanayagam, Y. B. Cheung, S. Matsumura, J. Chua, R. E. K. Man, K. Ohno-Matsui, T. Y. Wong, C. Y. Cheng, E. S. Tai, E. L. E. D. Lamoureux, L. Schmetterer, A. Kuo, Q. V. Hoang, and S. M. Saw, "Prevalence, risk factors and impact of posterior staphyloma diagnosed from wide-field optical coherence tomography in Singapore adults with high myopia," *Acta Ophthalmol.* **99**, e144 (2021).
29. N. K. Wang, Y. M. Wu, J. P. Wang, L. Liu, L. Yeung, Y. P. Chen, Y. H. Chen, L. K. Yeh, W. C. Wu, L. H. Chuang, and C. C. Lai, "Clinical characteristics of posterior staphylomas in myopic eyes with axial length shorter than 26.5 millimeters," *Am. J. Ophthalmol.* **165**, 199–200 (2016).
30. J. M. Pope, P. K. Verkicharla, F. Sepehrband, M. Suheimat, K. L. Schmid, and D. A. Atchison, "Three-dimensional MRI study of the relationship between eye dimensions, retinal shape and myopia," *Biomed. Opt. Express* **8**(5), 2386 (2017).

31. R. Frisina, I. Gius, M. Palmieri, A. Finzi, L. Tozzi, and B. Parolini, "Myopic traction maculopathy: Diagnostic and management strategies," *Clin. Ophthalmol.* **14**, 3699–3708 (2020).
32. S. Matsumura, C. Sabanayagam, C. W. Wong, C. S. Tan, A. Kuo, Y. L. Wong, K. Ohno-Matsui, T. Y. Wong, C. Y. Cheng, Q. V. Hoang, and S. M. Saw, "Characteristics of myopic traction maculopathy in myopic Singaporean adults," *Br. J. Ophthalmol.* **104**, 316182 (2020).
33. Q. V. Hoang, C. L. Chen, J. Garcia-Arumi, P. R. Sherwood, and S. Chang, "Radius of curvature changes in spontaneous improvement of foveoschisis in highly myopic eyes," *Br. J. Ophthalmol.* **100**(2), 222–226 (2016).
34. G. Sepúlveda, S. Chang, K. B. Freund, S. Park, and Q. V. Hoang, "Late recurrence of myopic foveoschisis after successful repair with primary vitrectomy and incomplete membrane peeling," *Retina* **34**(9), 1841–1847 (2014).
35. K. Devarajan, R. Sim, J. Chua, C. W. Wong, S. Matsumura, H. M. Htoon, L. Schmetterer, S. M. Saw, and M. Ang, "Optical coherence tomography angiography for the assessment of choroidal vasculature in high myopia," *Br. J. Ophthalmol.* **104**(7), 917–923 (2020).
36. N. Y. Q. Tan, C. C. A. Sng, and M. Ang, "Myopic optic disc changes and its role in glaucoma," *Curr. Opin. Ophthalmol.* **30**(2), 89–96 (2019).
37. N. Y. Q. Tan, C. C. A. Sng, J. B. Jonas, T. Y. Wong, N. M. Jansonius, and M. Ang, "Glaucoma in myopia: diagnostic dilemmas," *Br. J. Ophthalmol.* **103**, 1347 (2019).